Materials Advances

ROYAL SOCIETY OF CHEMISTRY

PAPER

View Article Online
View Journal | View Issue

Cite this: *Mater. Adv.*, 2022, 3, 1772

Excitation induced asymmetric fluorescence emission in 2D-WS_2 quantum dots

Wenjing Miao, Xinwen Gai, Fengyang Zhao and Jingang Wang *

Received 13th December 2021,
Accepted 11th January 2022

DOI: 10.1039/d1ma01178b

rsc.li/materials-advances

In this work, we synthesized 3–7 nm diameter tungsten disulfide quantum dots (WS_2 QDs) by pulsed laser ablation in ethanol solvent, and observed strong, stable, excitation independent blue emission. To further verify the luminescence mechanism of WS_2 QDs, EG-WS_2 QDs were prepared using ethylene glycol as a passivating agent in the experiment. Finally, we use theoretical calculations to prove the quantum mechanical mechanism of absorption and fluorescence emission. Theoretical studies have shown that the excellent fluorescence emission of WS_2 QDs is essentially symmetry breaking emission, and this mechanism determines its high fluorescence yield.

1. Introduction

In the past ten years, pioneering work on single-atom layer graphene has paved the way for the study of other two-dimensional layered van der Waals crystals.[1,2] Graphene is a kind of semiconductor with a zero-band gap structure, which hinders its application in fluorescence imaging and optoelectronic devices and provides impetus for the research of a new generation of fluorescent materials and electronic materials.[3–6] In addition to graphene, the research on fluorescence emission spectra has been extended to other two-dimensional nanomaterials, such as transition metal disulfides (TMDs),[7] hexagonal boron nitride (h-BN) and black phosphorus (BP).[5] As a typical TMD semiconductor, tungsten disulfide (WS_2) is a hexagonal structure composed of covalently bonded S–W–S three layers of atoms through van der Waals forces.[7–9] Because W has a large atomic number, it can effectively absorb X-rays and is used as a CT imaging contrast agent. In addition, the large interlayer spacing of WS_2 basically does not destroy its crystal structure when Li^+ is embedded, so it has potential application value in Li^+ batteries. In addition, WS_2 nanosheets have extremely strong friction properties and are widely used as lubricants, often appearing in large-scale machinery and equipment. However, WS_2 nanosheets have poor water solubility and weak fluorescence emission, which limits their further applications.[10,11] When the size of WS_2 nanosheets is reduced to less than 10 nm to form WS_2 QDs, due to the quantum confinement effect, the band gap will change from an indirect band gap (1.3 eV) to a direct band gap (2.1 eV), which can be improved. Fluorescence emission signal has potential application value in biological imaging.[12–15]

The currently reported preparation methods of WS_2 QDs include ion intercalation, ultrasonic-assisted peeling, electrochemical, solvothermal and hydrothermal methods. However, strict preparation conditions and the use of a variety of chemical reagents often introduce some impurities, which confuses the research of WS_2 QDs fluorescent transmitter. Unlike traditional organic dyes and inorganic quantum dots (such as CdS QDs and PbS QDs),[16–18] WS_2 QDs has less research on the fluorescence emission mechanism, which hinders its further application. In addition, the currently obtained WS_2 QDs quantum dot materials are mainly focused on the study of excitation-dependent fluorescence emission. There are few reports on strong, stable and excitation-independent fluorescence emission of WS_2 QDs, and no clear fluorescence emission mechanism has been obtained.

In this works, we use pulsed laser ablation to prepare water-soluble WS_2 QDs in ethanol solvent. The quantum dots show strong, stable, and excitation-independent fluorescence emission. This is because the electrons of WS_2 QDs are from the lowest unoccupied molecular energy.[19,20] Electronic transition from LUMO level (LUMO) to the highest occupied molecular level (HOMO) lower than the HOMO molecular energy level. The measured fluorescence quantum yield is as high as 26.6%. In the process of preparing WS_2 QDs by laser ablation, the laser beam acts on the ethanol molecules and the bulk WS_2 simultaneously, so that the cracked ethanol molecules are quickly passivated to the surface and edges of the WS_2 QDs, thereby forming a large number of oxygen-containing functional groups. These functional groups donate electrons to the central WS_2 nanodomain, causing its electron density to increase sharply until it reaches saturation. At this time, the band gap of WS_2 QDs is no longer sensitive to the quantum size effect, so that excitation-independent fluorescence emission signals are observed. To further verify the rationality of the fluorescence

College of Science, Liaoning Petrochemical University, Fushun 113001, China.
E-mail: jingang_wang@lnpu.edu.cn

emission mechanism of WS_2 QDs, EG-WS_2 QDs were prepared using ethylene glycol as the passivation agent in the experiment. The excitation independent fluorescence emission signal was also observed, which verified the correctness of the fluorescence emission mechanism of WS_2 QDs. It provides a theoretical basis for the application of WS_2 QDs in biological imaging, sensing and optoelectronic devices.

2. Method

2.1 Preparation of WS_2 QDs

First, place the WS_2 block on the bottom of a cuvette containing ethanol, fix the cuvette on the three-dimensional control table, and adjust the XYZ direction to focus the pulsed laser beam on the sample surface for ablation, and obtain a yellow-green WS_2 QDs solution. Finally, the WS_2 QDs solution can be obtained by centrifugation and transferred to a glass reagent bottle for sealed storage. In addition, under the condition that other conditions remain unchanged, ethylene glycol is used as a solvent to prepare WS_2 QDs with different fluorescence emission. During the experiment, the output wavelength of the Nd: YAG pulsed laser is 1064 nm, the repetition frequency is 10 Hz, the pulse width is 3–6 ns, the power density is about 200 mW cm^{-2}, and the ablation time is 20 min.

2.2 Characterization technique

The transmission electron microscope uses the JEM2100 transmission electron microscope produced by Japan JEOL to test the morphology, microstructure and size distribution of WS_2 QDs. Pipette 10 μL of WS_2 QDs solution and drop it on a 200-mesh ultra-thin carbon support film copper net, and dry it in a vacuum drying oven at 80 °C for 2 hours. The atomic force microscope (AFM) uses the XE-100 atomic force microscope produced by Park Systems in Germany to test the morphology and height of WS_2 QDs. 100 μL of WS_2 QDs solution was dropped on the silicon wafer substrate, and then the sample was spin-coated at a spin-coating rate of 1500 rpm. Finally, place the sample in a vacuum drying oven at 60 °C for 24 hours. Raman spectroscopy uses the model H13325 Raman spectrometer produced by British Renishaw Company to analyze the fine structure of WS_2 QDs. The excitation light wavelength is 532 nm, the grating is 2400 gr mm^{-1}, and the excitation light power is 1.0 mW. X-Ray photoelectron spectroscopy (XPS) uses the ESCALAB 250 X-ray spectrometer produced by Thermo-Fisher in the United States to analyze the chemical element composition and corresponding valence states of WS_2 QDs. The X-ray source is a monochromatic Al target source. The prepared XPS test sample was dropped on the silicon wafer substrate. Fourier infrared spectroscopy (FTIR) uses a Fourier infrared spectrometer model Nicolet iS10 produced by American Thermo Company to analyze the surface functional groups of WS_2 QDs. Drop 50 μL of WS_2 QDs solution directly on the KBr sheet, and then place it in the Fourier infrared spectroscopy cell for testing. The test wave number range of Fourier Infrared Spectrometer is 600–4000 cm^{-1}. Ultraviolet-visible absorption spectroscopy (UV-vis) was tested on the UV-vis absorption spectra of WS_2 QDs with a model TU-1901 ultraviolet-visible absorption spectrophotometer produced by Beijing Purse General Company. Pipette 2 mL of WS_2 QDs solution into a cuvette and use the corresponding solvent as a blank control group to test the UV-vis absorption spectrum of WS_2 QDs. Fluorescence spectroscopy (FL) was tested on the fluorescence emission spectra of WS_2 QDs using a fluorescence spectrophotometer model F-7000 produced by Hitachi, Japan. Pipette 2 mL of WS_2 QDs solution into a fluorescent cuvette, and gradually increase the excitation wavelength to test the fluorescence emission spectrum of WS_2 QDs.

2.3 Computational details

The quantum chemical calculations are performed by Gaussian 16.[21] The molecular structure is optimized using the B3LYP functional[22] in the density functional theory (DFT)[23] method in combination with the def2-TZVP basis set[24] with SDD effective core potential[25] and DFT-D3 correction method. The time-dependent DFT (TDDFT) method is used to combine the Cam-B3LYP functional[26] and the def2-TZVP basis set with SDD effective core potential for the excited state calculation by the optimized structure, and all the configuration coefficients were output. Based on this, the Multiwfn 3.6 program[27] is used for frontier molecular orbital drawing with the VMD program.[28]

3. Results and discussions

3.1 Structure of WS_2 QDs

Fig. 1(a) is a transmission electron microscope image of uniformly dispersed WS_2 QDs with a size distribution of 3–7 nm, and the size of most quantum dots is about 4 nm. As shown in Fig. 1(b and c), the WS_2 QDs obtained by pulsed laser ablation still have highly ordered lattice fringes, with fringe spacing of 0.20 nm and 0.61 nm, respectively, which are attributed to the WS_2 crystal. The (006) and (002) crystal planes in the middle indicate that the WS_2 QDs synthesized by the pulsed laser ablation method still have a hexagonal lattice structure. Here, a detailed presentation about the formation process of WS_2

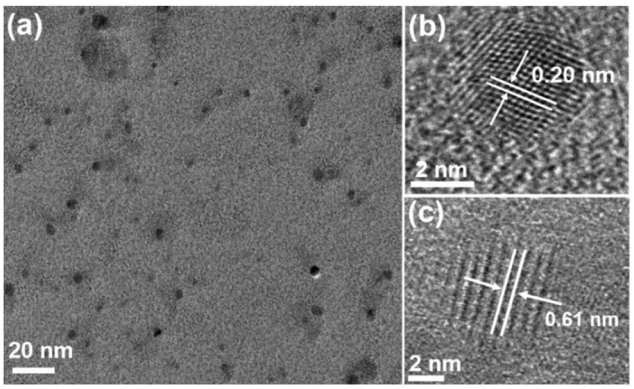

Fig. 1 (a) TEM image of WS_2 QDs; (b and c) HRTEM images of WS_2 QDs respectively.

QDs by pulsed laser ablation is presented as followed. Coulomb explosion occurs, and high thermionic electron emission produces a plasma plume with high temperature, high pressure and extreme high intensity of local electromagnetic fields when the laser beam pulses irradiate the bulk WS_2 dispersed in ethylene glycol solution. The micro zone of the WS_2 nanosheet is cracked and cut to form the WS_2 nano-cluster domain due to absorption of high enough energy. Simultaneously, ethylene glycol molecules adjacent to the WS_2 nano-cluster domain are also pyrolyzed by the high temperature to form oxygen-containing and nitrogen-containing substituents. At this time, C atoms with high surface energy at the periphery of WS_2 nano-cluster domain rapidly combine with pyrolyzed substituents (oxygen-containing and nitrogen-containing substituents). Thus, the WS_2 nano-cluster domain modified by abundant substituents forms WS_2 QDs with a passivation layer.

Fig. 2 is an atomic force microscope image of WS_2 QDs and a statistical diagram of the height distribution along the line. As shown in Fig. 2(a), the height of WS_2 QDs is less than 3 nm. As shown in Fig. 2(b), the heights of WS_2 QDs were tested along the red and green lines in Fig. 2(a). The results showed that the heights of these WS_2 QDs were 1.74 nm, 1.03 nm, 1.49 nm and 1.67 nm, respectively. The height of most quantum dots is about 1.22 nm, which indicates that the WS_2 QDs obtained by ablating the WS_2 block along the direction parallel to the layer have a single-layer or double-layer structure.

To analyze the chemical composition and atomic valence of WS_2 QDs, we performed XPS spectral characterization. As shown in Fig. 3(a), the WS_2 QDs mainly contain four elements: tungsten, sulfur, carbon and oxygen. Among them, carbon and oxygen may come from the passivation of the surface of WS_2 QDs by ethanol solvent molecules. Fig. 3(b) is the W^{4+} high-resolution XPS spectrum of WS_2 QDs. It can be clearly seen that there are two peaks at 32.8 eV and 34.7 eV, which are related to the binding energy of W^{4+}, while those near 36 eV and 38.6 eV The two peaks are respectively related to the binding energy of W^{6+}. In addition, as shown in Fig. 3(c), the $S2p_{3/2}$ and $S2p_{1/2}$ peaks appear at binding energies of 162.2 eV and 163.6 eV, respectively, and they correspond to the characteristic peaks of −2 valence S. The peak at 169.3 eV is related to S^{6+}, indicating that some S atoms oxidize from −2 to +6. The above results indicate that W–O bonds and S–O bonds are formed on the surface and edges of WS_2 QDs during laser ablation. In order to

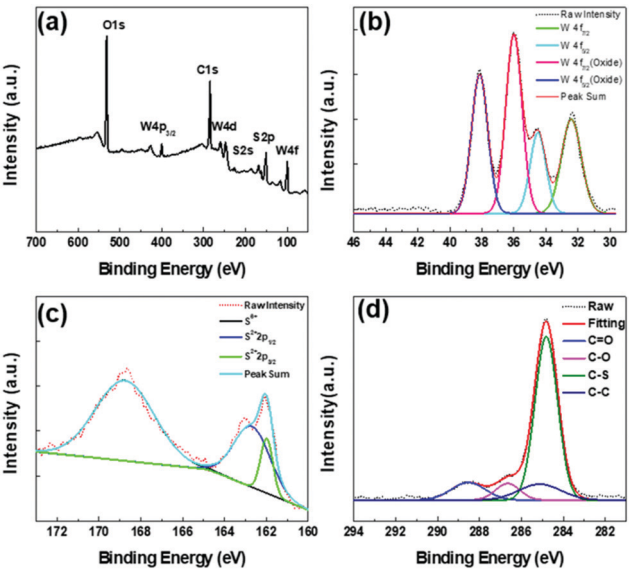

Fig. 3 (a) XPS spectrum of WS_2 QDs; (b) high resolution W4f spectrum of WS_2 QDs; (c) high resolution S_2p spectrum of WS_2 QDs; (d) high resolution C1s spectrum of WS_2 QDs.

provide further information on the surface structure of WS_2 QDs, the high-resolution C1s spectra of WS_2 QDs are also given. As shown in Fig. 3(d), the C1s high-resolution electron binding energy spectrum of WS_2 QDs is fitted to form four Lorentz singlets, which are located at 284.2 eV, 284.6 eV, 286.8 eV and 288.2 eV, which are attributed in turn the C═C bond, C–S bond, C–O bond and C═O bond indicate that there are abundant oxygen-containing functional groups and sulfur-containing functional groups in WS_2 QDs.

To further determine the microstructure of WS_2 QDs, we conducted Raman and Fourier infrared spectroscopy tests. As shown in Fig. 4(a), two Raman characteristic peaks can be clearly observed in the Raman spectrum of WS_2 QDs. The front peak is located at 415 cm^{-1}, which can be attributed to the phonon mode E_{2g} and the rear peak at 350 cm^{-1}, it can be attributed to the out-of-plane phonon vibration mode A1g, which indicates that WS_2 QDs have a hexagonal crystal structure. Compared with the WS_2 block, the Raman peaks corresponding to E_{2g} and A_{1g} of WS_2 QDs have redshifts of 4.1 cm^{-1} and 3.2 cm^{-1}, respectively, indicating that WS_2 QDs is a

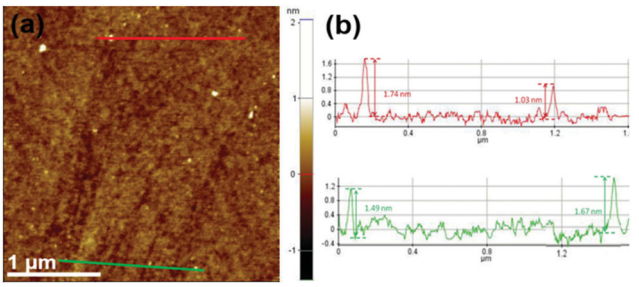

Fig. 2 (a) AFM diagram of WS_2 QDs; (b) height distribution statistics curve of WS_2 QDs along the red and green lines in (a).

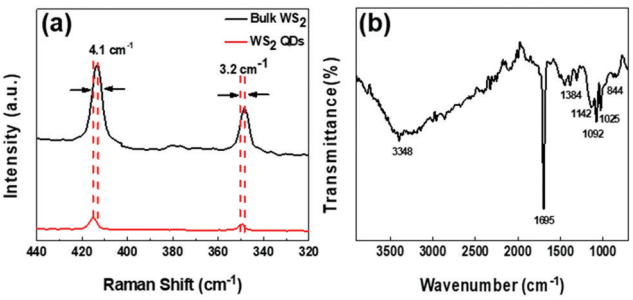

Fig. 4 (a) Comparison of Raman spectra of bulk WS_2 and WS_2 QDs; (b) Fourier infrared spectra of WS_2 QDs.

single-layer structure or its interlayer van der Waals force Decrease. As shown in Fig. 4(b), the broad peak at 3348 cm^{-1} is attributed to the stretching vibration of the O–H bond. The peak at 1695 cm^{-1} is attributed to the formation of the C=O double bond. The weaker peaks at 1142 cm^{-1} and 844 cm^{-1} are attributed to the stretching vibration of the S–OH bond. In addition, the peaks at 1092 cm^{-1} and 1384 cm^{-1} are attributed to the stretching vibration of the W=O double bond and the stretching vibration of the W–OH bond, respectively, indicating that the W atoms at the edge and surface of WS_2 QDs are partially Oxidation.

3.2 Optical properties of WS_2 QDs

As shown in Fig. 5(a), there is an obvious strong peak in the photoluminescence spectrum of WS_2 QDs at 445 nm, and another weak shoulder peak at 422 nm. These two fluorescence emission belong to the blue emission band. By monitoring the fluorescence peak at 445 nm, the best excitation peak center of WS_2 QDs can be obtained at 375 nm. At this time, the shift between the best excitation peak and the best fluorescence emission peak is 70 nm. As shown in Fig. 5(b), the photoluminescence peak position of WS_2 QDs prepared by laser ablation method does not move with the increase of excitation wavelength, and the center is always stable at 445 nm. With the excitation wavelength from 320 nm to 380 nm, the fluorescence emission signal of WS_2 QDs first increases and then decreases. The fluorescence emission intensity reaches the maximum when the excitation wavelength is 370 nm. In order to further study the source of fluorescence emission, the fluorescence emission excitation spectrum of WS_2 QDs was fitted with Lorentz to obtain two obvious excitation bands (green lines), their centers were located at 365 nm (about 3.39 eV) and 382 nm (about 3.24 eV) (as shown in Fig. 5(c)). The fluorescence quantum yield of the tested WS_2 QDs can reach 18.64%, which has good luminous efficiency. In addition, as shown in Fig. 5(d), the fluorescence emission spectra of WS_2 QDs are also fitted to form two emission bands, the centers of which are located at 419 nm and 448 nm, respectively. By further calculating the energy band of the excitation spectrum, it can be obtained that the energy difference between 365 nm and 382 nm is 0.15 eV, which is exactly the same as the photoluminescence spectrum at 425 nm (about 2.91 eV) and 448 nm (about 2.76 eV) The energy difference (0.15 eV) is equal.

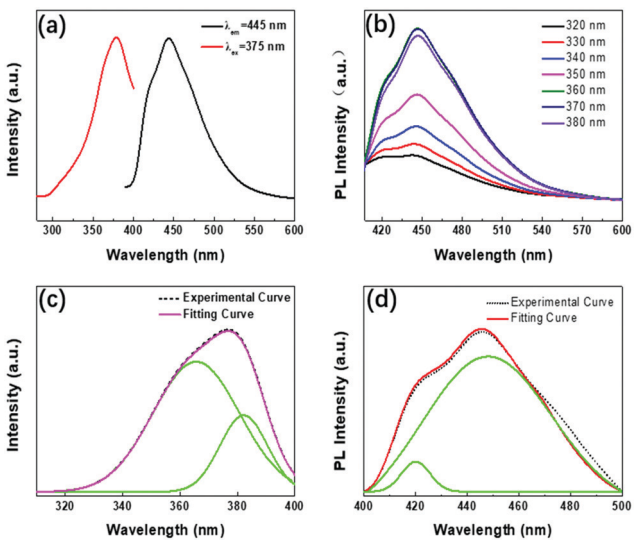

Fig. 5 (a) Absorption and photoluminescence spectra of WS_2 QDs dispersed in ethanol solvent; (b) photoluminescence spectra of WS_2 QDs with increasing excitation wavelength; (c) monitoring at 445 nm Fluorescence emission peak, get the photoluminescence excitation spectrum of WS_2 QDs (dotted line) and the fitted Lorentz spectrum; (d) the photoluminescence excitation spectrum of WS_2 QDs (dotted line) and the fitted Lorentz spectrum line.

As mentioned above, the peak positions of PL emission remain un-shifted as the excitation wavelength changes from 320 nm to 380 nm (Fig. 5b). In generally, PL emission of WS_2 QDs is probably derived from electron transitions of the intrinsic state, or the surface/edge state. To clearly clarify PL mechanism of WS_2 QDs, PLE spectrum is measured by montoring the PL emission band centered at 448 nm, and then is fitted into two primary components (green curves) located at 365 nm (~3.39 eV) and 382 nm (~3. 24 eV) by Lorentzian function in Fig. 5a, respectively. In PLA process, the local high temperature pyrolyzes bulk WS_2 precursor into WS_2 nanoclusters which have many dangling bonds on the periphery and surface. Meanwhile, ethanol solvent is pyrolyzed into oxygen-containing functional groups which directly passivate the edges and surfaces of WS_2 nanoclusters to form passivation layer structures. Which directly passivate the edges and surfaces of WS_2 nanoclusters to form passivation layer structures. Thus, WS_2 QDs possess a broad energy band so as to provide more probability in the electron transition process. On the other hand, excited electrons can recombine with holes to generate the strong PL emission after vibrational relaxation. It is necessary to emphasize that the broad absorption band are possibly originated from electron contribution of luminophor, rather than from that of the WS_2 nanocluster in UV-vis absorption spectrum of WS_2. As shown in the Fig. 5(c and d), the energy difference corresponding to the two peaks at 365 nm (3.39 eV) and 382 nm (3.24 eV) is 0.15 eV, and the energy difference corresponding to the two peaks at 425 nm (2.91 eV) and 448 (2.76 eV) nm is 0.15 eV by calculating the fitted peaks in the PLE spectrum. Thus, it is again certified that double PL emission peaks are originated from transitions of electron from the LUMO energy level to the HOMO energy level and energy levels below the HOMO1, respectively. The double energy levels are possibly related to the luminophors (W=O, S–OH, W–O–C, *etc.*) which are also called electron-donating functional groups. The oxygen-containing functional groups can donate electrons to the WS_2 nanocluster to cause the increase of the charge densities. Therefore, the energy levels of WS_2 QDs rise and the band gap becomes narrow. Ultimately, the band gaps of WS_2 QDs remain unchanged due to the saturated passivation, and is insensitive to size. Thus, the excitation-wavelength independent PL emission is observed in violet-blue region.

This photoluminescence excitation spectrum composed of dual excitation bands provides a necessary theoretical basis for

further understanding of the luminescence mechanism of WS_2 QDs. Therefore, the fluorescence peak of WS_2 QDs comes from the transition of electrons from the lowest unoccupied molecular energy level (LUMO) to the highest occupied molecular energy level (HOMO) and the H_1 energy level lower than the HOMO molecular energy level. Similar to C-QDs and BP-QDs, the fluorescence emission of WS_2 QDs is likely to be related to oxygen-containing functional groups. When the pulsed laser ablated the bulk WS_2 in ethanol solvent, the high temperature and high pressure generated by the local high-energy laser beam quickly destroyed the W–S covalent bond in the WS_2 layer and the van der Waals force between the layers, forming nano-WS_2 domains. At the same time, the oxygen-containing functional groups formed by thermal decomposition of ethanol solvent molecules quickly saturate and passivate on the surface and edge of the WS_2 domain, forming electron-donating substituents on its edges. Due to the saturation passivation, the electron donating ability of the groups on these surfaces is enhanced, and the electrons are transferred from the functional groups to the WS_2 QDs, resulting in an increase in the charge density, an increase in the highest occupied orbital, and a decrease in the band gap. Due to the saturation passivation, the size change of the band gap WS_2 QDs is insensitive and reaches a stable value, so that strong, stable and excited independent blue emission is observed. As showen in Fig. 6.

3.3 Luminescence characteristics of passivated WS_2 QDs

To further verify the fluorescence emission mechanism of WS_2 QDs, EG-WS_2 QDs samples were prepared by replacing ethylene glycol as the passivating agent under the same conditions. Similar to the WS_2 QDs passivated by ethanol, the EG-WS_2 QDs passivated by ethylene glycol are still uniformly dispersed, with a size distribution of 3–7 nm. The size of most quantum dots is about 4 nm (Fig. 7(a) shows), indicating that the solvent has no major influence on the size of EG-WS_2 QDs. Fig. 7(b and c) are the HRTEM of EG-WS_2 QDs. From the figure, it can be observed that EG-WS_2 QDs have highly ordered lattice fringes. The fringe spacing is 0.21 nm and 0.61 nm, which are attributed to the (006) and (002) crystal planes in the WS_2 crystal indicate that the lattice structure of the EG-WS_2 QDs passivated by ethylene glycol remains unchanged and still has a hexagonal lattice structure.

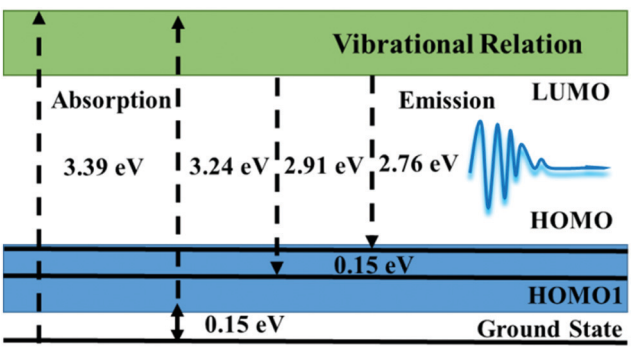

Fig. 6 PL emission mechanism profile of WS_2 QDs.

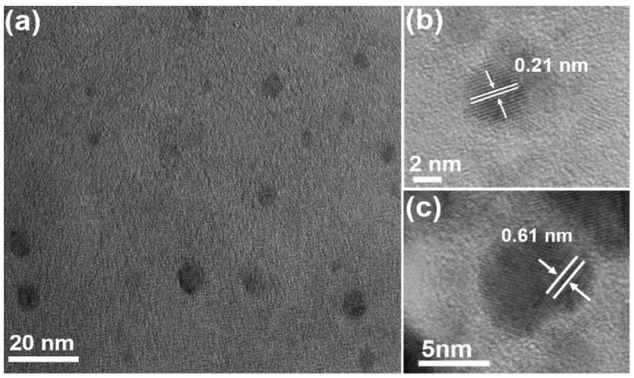

Fig. 7 (a) TEM image of EG-WS_2 QDs; (b and c) HRTEM image of EG-WS_2 QDs respectively.

As shown in Fig. 8(a), similar to the WS_2 QDs passivated by ethanol solvent, two Raman characteristic peaks can be clearly observed in the Raman spectrum of EG-WS_2 QDs passivated by ethylene glycol, respectively at 415 cm^{-1} and 350 cm^{-1}, the EG-WS_2 QDs passivated by ethylene glycol have the same hexagonal structure as the bulk WS_2. In order to further analyze the chemical composition and surface structure of EG-WS_2 QDs, we carried out XPS and Fourier infrared spectroscopy tests respectively. In the W4f high-resolution XPS spectrum of EG-WS_2 QDs, two weaker binding energy peaks can be observed, located at 32.6 eV and 34.5 eV, respectively, which are related to the binding energy of W^{4+}. The two strong peaks at 36.2 eV and 38.4 eV are both related to the binding energy of W^{6+} (as shown in Fig. 8(b)). As shown in Fig. 8(c), the binding energy peaks of $S2p_{3/2}$ and $S2p_{1/2}$ are located at 162.1 eV and 163.8 eV, respectively, which correspond to the characteristic peaks of −2 valence S. At the same time, the binding energy peak at 169.5 eV is related to the characteristic peak of S with +6 valence, indicating that part of the S atoms are also oxidized

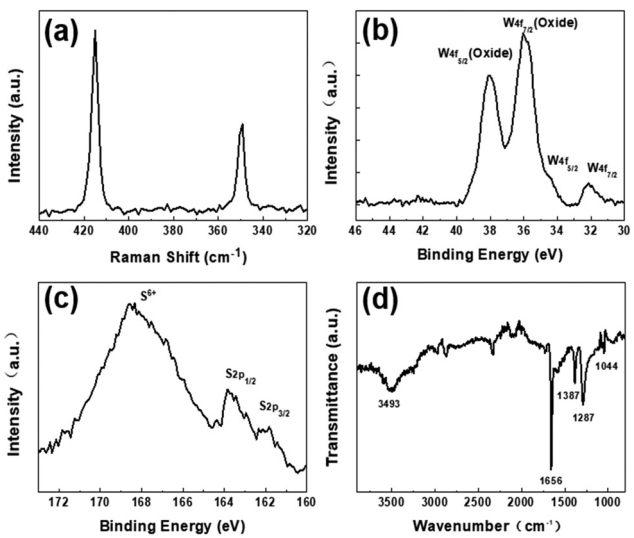

Fig. 8 (a) Raman spectrum of EG-WS_2 QDs; (b) high resolution W4f XPS spectrum of EG-WS_2 QDs; (c) High resolution S2p XPS spectrum of EG-WS_2 QDs; (d) EG-Fourier infrared spectrum of WS_2 QDs.

by the solvent during the laser ablation process. In addition, as shown in Fig. 8(d), the broad peak at 3493 cm^{-1} is attributed to the O–H stretching vibration. The peak at 1656 cm^{-1} is attributed to the stretching vibration of C=O. The peaks at 1387 cm^{-1}, 1287 cm^{-1}, and 1044 cm^{-1} are all attributed to W–OH stretching vibration. Compared with the EG-WS_2 QDs passivated by ethanol, the W atoms on the surface and edges of the EG-WS_2 QDs passivated by ethylene glycol are passivated by more oxygen-containing groups. At the same time, the EG-WS_2 QDs Without the W=O bond, this difference in surface structure will result in different fluorescence emission.

As shown in Fig. 9(a), the fluorescence emission peak of EG-WS_2 QDs exhibits excitation-independent characteristics, that is, the emission wavelength does not move with the increase of excitation wavelength, and the central peak position is always stable at 450 nm. With the excitation wavelength from 320 nm to 390 nm, the fluorescence emission signal intensity of EG-WS_2 QDs first increases and then decreases. When the excitation wavelength is 380 nm, the fluorescence emission intensity of EG-WS_2 QDs reaches the maximum. Comparing the fluorescence emission peaks of EG-WS_2 QDs and E-WS_2 QDs, it is found that the fluorescence emission peaks of EG-WS_2 QDs have a red shift of 5 nm. Similar to the CQDs in Chapter 3, the structure of EG-WS_2 QDs is composed of WS_2 domains and surface functional groups. In fact, different solvents have no effect on the WS_2 domain with a hexagonal lattice structure in the center. However, the surface functional group chains of EG-WS_2 QDs and E-WS_2 QDs are not the same, leading to differences in their fluorescence emission. When using laser ablation to prepare WS_2 QDs, the laser beam splits the WS_2 crystal and solvent molecules at the same time. Generally speaking, ethylene glycol molecules have longer molecular chains, so the ethylene glycol molecules after cleavage passivation have longer molecular chains on the surface of EG-WS_2 QDs, which means that the size of EG-WS_2 QDs is larger. On the other hand, compared with the energy level of E-WS_2 QDs, the HUMO energy level of EG-WS_2 QDs further increases until it reaches saturation. The band gap widths of EG-WS_2 QDs and E-WS_2 QDs are basically unchanged and very close, The energy level difference is only 0.03 eV. Therefore, the fluorescence emission of E-WS_2 QDs and EG-WS_2 QDs are derived from the transition of electrons from the lowest unoccupied molecular energy level (LUMO) to the highest occupied molecular energy level (HOMO) and the H1 energy level lower than the HOMO molecular energy level. In addition, the fluorescence quantum yield of the obtained CQDs is as high as 26.6%, showing good luminescence performance, which lays the foundation for further application to cell biological imaging.

3.4 Physical mechanism of excitation, fluorescence, and orbitals

Fig. 10(a) shows the absorption spectrum and fluorescence spectrum calculated by DFT. It can be found from the figure that the theoretically calculated spectrum is very close to the experimental spectrum (Fig. 5). Therefore, it can be explained that the theoretical calculation and analysis are basically consistent with the actual situation. Fig. 10b shows the frontier molecular orbitals of WS_2 QDs.

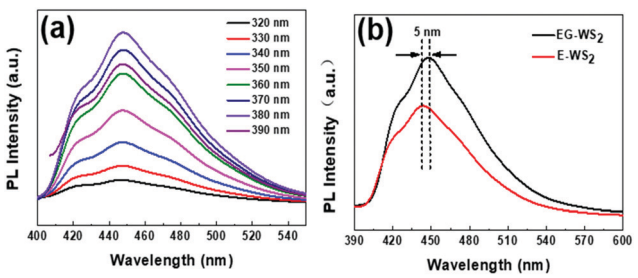

Fig. 9 (a) Photoluminescence spectra of EG-WS_2 QDs with excitation from 320 nm to 390 nm; (b) Fluorescence spectra of EG-WS_2 QDs and ethanol passivated WS_2 QDs (E-WS_2 QDs).

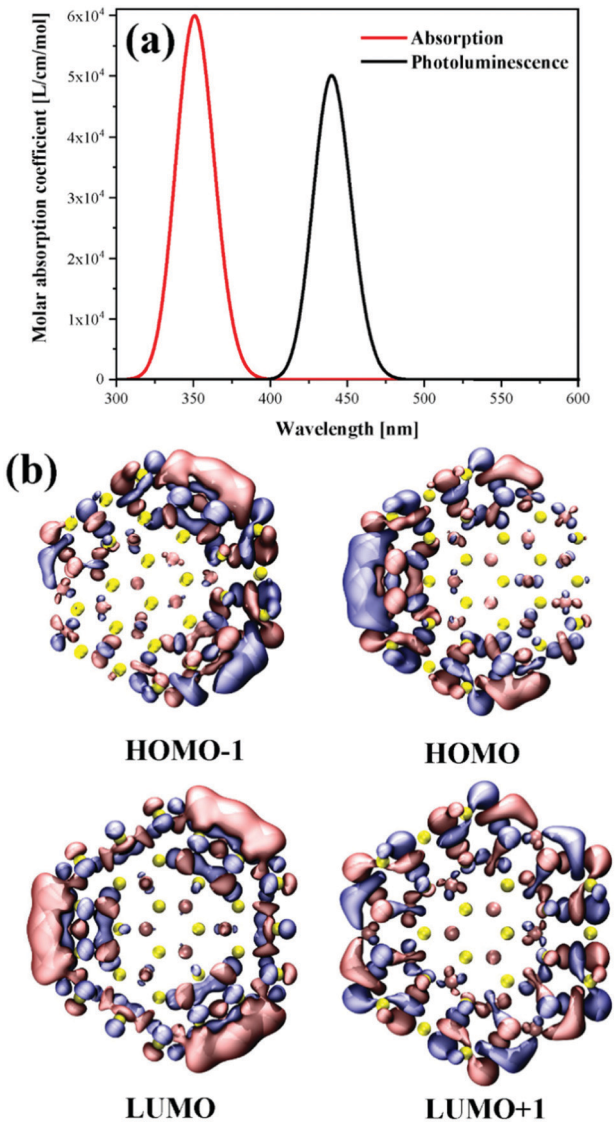

Fig. 10 (a) The calculated absorption and fluorescence spectra. (b) Frontier molecular orbitals of WS_2 QDs.

The upper half is the highest occupied orbits HOMO−1 and HOMO. It can be found that the main orbits are mainly distributed on the boundary, and a relatively large delocalized orbit is gathered on one side. HOMO−1 and HOMO are degenerate. The symmetrical WS_2 QDs length produces asymmetric HOMO orbitals, which is a symmetry breaking phenomenon. However, the two occupied orbitals are clearly degenerate. Because from the formal point of view, the two orbits are extremely similar after a certain symmetry inversion. On the other hand, LUMO and LUMO+1 are completely symmetrical orbitals and are still distributed on the boundary of QDs. This excitation of transition from symmetry broken orbit to symmetric orbit is a kind of light-induced wave function summarization. The fluorescence emission is a symmetry breaking radiation. Therefore, the fluorescence efficiency of WS_2 QDs is very high.

4. Conclusions

In this work, firstly, WS_2 QDs were prepared by pulsed laser ablation in ethanol solvent, and strong, stable, excited independent blue emission was observed. This fluorescence emission that does not move with the excitation wavelength is attributed to the electronic transition from the lowest unoccupied molecular orbital (LUMO) to the highest occupied molecular orbital (HOMO). In the process of preparing WS_2 QDs by laser ablation, the laser beam acts on the ethanol molecules and the bulk WS_2 simultaneously, so that the cracked ethanol molecules are quickly passivated to the surface and edges of the WS_2 QDs, thereby forming a large number of oxygen-containing functional groups. These functional groups donate electrons to the central WS_2 nanodomain, causing its electron density to increase sharply until it reaches saturation. At this time, the band gap of WS_2 QDs is no longer sensitive to quantum size effects and exhibits excitation-independent fluorescence emission characteristics. To further verify the luminescence mechanism of WS_2 QDs, EG-WS_2 QDs were prepared using ethylene glycol as a passivating agent in the experiment. Finally, through theoretical calculations, it is found that the transition from symmetry broken orbit to symmetrical orbit is a kind of light-induced wave function summarization. The fluorescence emission is a symmetry breaking radiation. Therefore, the fluorescence efficiency of WS_2 QDs is extremely high.

Author contributions

Jingang Wang and Fengyang Zhao; conceptualization; methodology, Jingang Wang; investigation, Jingang Wang; writing – original draft preparation, Wenjing, Miao and Xinwen Gai.

Conflicts of interest

There are no conflicts to declare.

Acknowledgements

This work was financially supported by the National Natural Science Foundation of China (No. 21808096); the Scientific research fund project of education department of liaoning province (No. L2019028).

References

1 A. K. Geim and I. V. Grigorieva, van der Waals heterostructures, *Nature*, 2013, **499**, 419–425.
2 F. Withers, O. D. Pozo-Zamudio, A. Mishchenko, A. P. Rooney, A. Gholinia, K. Watanabe, T. Taniguchi, S. J. Haigh, A. K. Geim and A. I. Tartakovskii, Light-emitting diodes by band-structure engineering in van der Waals heterostructures, *Nat. Mater.*, 2015, **14**, 301–306.
3 J. Wang, F. Ma and M. Sun, Graphene, hexagonal boron nitride, and their heterostructures: properties and applications, *RSC Adv.*, 2017, **7**, 16801–16822.
4 J. Wang, F. Ma, W. Liang and M. Sun, Electrical properties and applications of graphene, hexagonal boron nitride (h-BN), and graphene/h-BN heterostructures, *Mater. Today Phys.*, 2017, **2**, 6–34.
5 J. Wang, X. Mu, X. Wang, N. Wang, F. Ma, W. Liang and M. Sun, The thermal and thermoelectric properties of in-plane C-BN hybrid structures and graphene/h-BN van der Waals heterostructures, *Mater. Today Phys.*, 2018, **5**, 29–57.
6 J. Wang, W. Bo, Y. Ding and X. Mu, Optical, Optoelectronic and Photoelectric Properties in Moiré Superlattices of Twisted Bilayer Graphene, *Mater. Today Phys.*, 2020, 100238.
7 S. Xu, D. Li and P. Wu, One-pot, facile, and versatile synthesis of monolayer MoS_2/WS_2 quantum dots as bioimaging probes and efficient electrocatalysts for hydrogen evolution reaction, *Adv. Funct. Mater.*, 2015, **25**, 1127–1136.
8 M. O. Valappil, A. Anil, M. Shaijumon, V. K. Pillai and S. Alwarappan, A Single-Step Electrochemical Synthesis of Luminescent WS2 Quantum Dots, *Chem. – Eur. J.*, 2017, **23**, 9144–9148.
9 M.-J. Kim, S.-J. Jeon, T. W. Kang, J.-M. Ju, D. Yim, H.-I. Kim, J. H. Park and J.-H. Kim, 2H-WS_2 Quantum dots produced by modulating the dimension and phase of 1T-nanosheets for antibody-free optical sensing of neurotransmitters, *ACS Appl. Mater. Interfaces*, 2017, **9**, 12316–12323.
10 H. Liu, J. Lu, K. Ho, Z. Hu, Z. Dang, A. Carvalho, H. R. Tan, E. S. Tok and C. H. Sow, Fluorescence concentric triangles: a case of chemical heterogeneity in WS_2 atomic monolayer, *Nano Lett.*, 2016, **16**, 5559–5567.
11 X. Zuo, H. Zhang, Q. Zhu, W. Wang, J. Feng and X. Chen, A dual-color fluorescent biosensing platform based on WS_2 nanosheet for detection of Hg^{2+} and Ag, *Biosens. Bioelectron.*, 2016, **85**, 464–470.
12 M. Kriegmair, A. Ehsan, R. Baumgartner, W. Lumper, R. Knuechel, F. Hofstädter, P. Steinbach and A. Hofstetter, Fluorescence photodetection of neoplastic urothelial lesions following intravesical instillation of 5-aminolevulinic acid, *Urology*, 1994, **44**, 836–841.
13 N. Lange, P. Jichlinski, M. Zellweger, M. Forrer, A. Marti, L. Guillou, P. Kucera, G. Wagnieres and H. Van Den Bergh, Photodetection of early human bladder cancer based on the

fluorescence of 5-aminolaevulinic acid hexylester-induced protoporphyrin IX: a pilot study, *Br. J. Cancer*, 1999, **80**, 185–193.

14 X. Mu, J. Wang and M. Sun, Visualization of photoinduced charge transfer and electron–hole coherence in two-photon absorption, *J. Phys. Chem. C*, 2019, **123**, 14132–14143.

15 X. Mu, H. Zong, L. Zhu and M. Sun, External electric field-dependent photoinduced charge transfer in a donor–acceptor system in two-photon absorption, The, *J. Phys. Chem. C*, 2020, **124**, 2319–2332.

16 F. Kröger and H. Vink, The origin of the fluorescence in self-activated ZnS, CdS, and ZnO, *J. Chem. Phys.*, 1954, **22**, 250–252.

17 A. Hässelbarth, A. Eychmüller and H. Weller, Detection of shallow electron traps in quantum sized CdS by fluorescence quenching experiments, *Chem. Phys. Lett.*, 1993, **203**, 271–276.

18 X. Mu, X. Wang, J. Quan and M. Sun, Photoinduced Charge Transfer in Donor-Bridge-Acceptor in One-and Two-photon Absorption: Sequential and Superexchange Mechanisms, *J. Phys. Chem. C*, 2020, **124**, 4968–4981.

19 Y. Zhong, Y. Shao, F. Ma, Y. Wu, B. Huang and X. Hao, Band-gap-matched CdSe QD/WS_2 nanosheet composite: Size-controlled photocatalyst for high-efficiency water splitting, *Nano Energy*, 2017, **31**, 84–89.

20 H. Long, L. Tao, C. P. Chiu, C. Y. Tang, K. H. Fung, Y. Chai and Y. H. Tsang, The WS_2 quantum dot: preparation, characterization and its optical limiting effect in polymethylmethacrylate, *Nanotechnology*, 2016, **27**, 414005.

21 M. Frisch, G. Trucks, H. Schlegel, G. Scuseria, M. Robb, J. Cheeseman, G. Scalmani, V. Barone, G. Petersson and H. Nakatsuji, *Gaussian 16*, Gaussian, Inc., Wallingford, CT, 2016.

22 A. D. Becke, Density-functional thermochemistry. IV. A new dynamical correlation functional and implications for exact-exchange mixing, *J. Chem. Phys.*, 1996, **104**, 1040–1046.

23 W. Kohn and L. J. Sham, Self-Consistent Equations Including Exchange and Correlation Effects, *Phys. Rev.*, 1965, **140**, A1133–A1138.

24 A. Schäfer, H. Horn and R. Ahlrichs, Fully optimized contracted Gaussian basis sets for atoms Li to Kr, *J. Chem. Phys.*, 1992, **97**, 2571–2577.

25 T. H. Dunning and P. J. Hay, Methods of electronic structure theory, in *Modern theoretical chemistry*, Plenum Press, New York, 1977, Vol. 3, p 1.

26 T. Yanai, D. P. Tew and N. C. Handy, A new hybrid exchange–correlation functional using the Coulomb-attenuating method (CAM-B3LYP), *Chem. Phys. Lett.*, 2004, **393**, 51–57.

27 T. Lu and F. Chen, Multiwfn: a multifunctional wavefunction analyzer, *J. Comput. Chem.*, 2012, **33**, 580–592.

28 W. Humphrey, A. Dalke and K. Schulten, VMD: visual molecular dynamics, *J. Mol. Graphics*, 1996, **14**, 33–38.